Journal of Magnetic Resonance **155,** 15–28 (2002)
doi:10.1006/jmre.2002.2503, available online at http://www.idealibrary.com on IDEAL®

# A Robust Technique for Two-Dimensional Separation of Undistorted Chemical-Shift Anisotropy Powder Patterns in Magic-Angle-Spinning NMR

S-F. Liu, J-D. Mao, and K. Schmidt-Rohr[1]

*Department of Chemistry and Ames Laboratory, Iowa State University, Ames, Iowa 50011*

Received June 4, 2001; revised December 17, 2001

**A robust magic-angle-spinning experiment for separating undistorted, quasi-static chemical-shift powder patterns is presented. It is derived from the technique of R. Tycko, G. Dabbagh, and P. Mirau (1989, *J. Magn. Reson.* 85, 265), but uses 360° instead of 180° pulses. In combination with a suitable phase sequence, this makes the spectral patterns very insensitive to pulse-length errors and other imperfections, as demonstrated both experimentally and theoretically. This method, termed *s*eparation of *u*ndistorted *p*owder patterns by *e*ffortless *r*ecoupling (SUPER), can be used at standard spinning speeds, between 2.5 and 5 kHz, and with standard radiofrequency power levels (in particular, for protons, a decoupling field strength $\gamma B_1/2\pi$ of less than 80 kHz). No significant artifacts are observed even for samples extending to the ends of the radiofrequency coil. The method has been applied to samples containing various $sp^2$- and $sp^3$-hybridized carbon sites. Even for the methylene groups in polyethylene, a system with very strong C–H and H–H dipolar couplings and only moderate chemical-shift anisotropy (CSA), a useful CSA powder pattern has been obtained. With a CSA scaling factor of 0.155, accuracies of ±5, ±3, and ±1 ppm of the principal values can be achieved for protonated aromatic carbons, unprotonated $sp^2$-hybridized groups, and aliphatic sites, respectively. Examples of CSA-based assignment of COOC vs other COO or CON groups, and of aromatic vs olefinic C=C carbons are shown, for both small molecules and polymers.** 

## INTRODUCTION

The chemical-shift anisotropy (CSA) is a useful observable in solid-state NMR, which can provide information not only on segmental orientations and reorientations (*1*) but also on the local structure of proteins (*2–4*) and other molecules (*5, 6*). With the continuing improvement of ab initio chemical-shift calculations, the CSA will become an ever more useful probe of molecular conformations (*2, 7*). The CSA is also useful for distinguishing different groups with overlapping isotropic-chemical-shift ranges. For instance, COOH and COOC groups both have isotropic shifts near 170 ppm, but their central ($\sigma_{22}$) chemical-shift principal values are systematically different by >30 ppm (*8*). A similar $\sigma_{22}$-based distinction is possible between aromatic and olefinic C=C carbons (*8*), or between bridgehead and other aromatic carbons (*5, 8*).

Nevertheless, the chemical-shift anisotropy has not been exploited nearly to its full potential. The reason has been the lack of a convenient, robust technique that yields chemical-shift powder patterns under standard magic-angle-spinning (MAS) conditions. In principle, if the spinning frequency $\omega_r$ is smaller than the chemical-shift anisotropy $\delta$, the two parameters $\delta$ and $\eta$ that characterize the chemical-shift anisotropy (*1*) can be extracted from the intensities of MAS sidebands (*9*). In sufficiently simple compounds, spinning sideband patterns can be determined for some sites in 1D spectra. For more complex systems, two-dimensional sideband-separation techniques using a limited number of pulses have also been developed (*10–14*). However, most of the known sideband-separation techniques must be performed at unusually low rotation frequencies $\omega_r < 2$ kHz and require complex schemes for pulse timings or data processing (*10–12*). It should also be noted that the MAS sideband analysis usually assumes that the anisotropy is ideal, i.e., that it reflects a single chemical-shift tensor and that no intermediate motion or partial orientation is present; these assumptions are difficult to test for sideband patterns with less than about seven significant sidebands.

Without sample rotation, the chemical-shift anisotropy produces characteristic powder patterns, with a peak at $\sigma_{22}$, the middle principal value of the chemical-shift tensor, and sharp steps at the two other principal values (*1*). With suitable rotation-synchronized radiofrequency pulses, such static powder patterns can also be produced in the first dimension of a 2D MAS experiment (*12, 15–21*). Such undistorted quasi-static powder patterns have several major advantages over MAS sideband patterns. First and foremost, the data analysis is very significantly simplified. The principal values can be read off with a cursor or ruler from the position of the peak and the two shoulders. This makes time-consuming simulations unnecessary. If simulations are desired, they are much simpler than those needed for MAS sideband patterns. Second, deviations from an ideal powder pattern due to intermediate-timescale motions, partial

[1] To whom correspondence should be addressed. E-mail: srohr@iastate.edu.



1090-7807/02 $35.00

orientation, or superposition of signals with different chemical-shift anisotropies can be recognized immediately, because only a small set of different ideal powder-lineshapes (*1*) are possible. Third, the quasi-static frequency dimension can be used to measure orientation distributions in oriented samples, and extensions to 3D DECODER orientation or exchange NMR dynamics measurements (*1*) are straightforward.

A few techniques for obtaining undistorted quasi-static CSA powder patterns under standard MAS conditions have been described (*16, 18, 19*), while others provide unusual powder patterns (*22–24*). Some methods are distortionless only for very small scaling factors (<0.1) (*16*), while most other CSA recoupling pulse sequences are notoriously sensitive to pulse-length imperfections or off-resonance effects (*18, 19, 22, 23*) or suffer from low sensitivity (*24*). The techniques that yield the best powder patterns require unconventional hardware for angle switching (*15, 17, 25*), for slow spinning, and/or for special rotor synchronization throughout the pulse sequence (*12, 20, 21*).

Thus, a simple technique that yields undistorted CSA powder patterns with high sensitivity and that works reliably at standard MAS conditions has remained elusive. The pulse sequence introduced here is designed to fill this gap. It is derived from the method by Tycko *et al.* (*18*). The technique of Tycko *et al.* is based on ingenious insight into, and clever manipulation of, the time-dependent frequency under MAS, but it is very sensitive to $B_1$ field inhomogeneities (*18*). It relies on four exact 180° pulses per rotation period; a variation in the $B_1$ field strength by only 10% was shown to lead to serious line broadening (*18*). Since, in practice, the sample at the ends of the coil will experience a 50% smaller $B_1$ field than in the center, for Tycko's technique the sample must be restricted to a very small region near the center of the coil, reducing the sample amount and thus the sensitivity.

The technique of Tycko *et al.* also produces serious artifacts at the limits of the spectral range (*18*). These are irrelevant for the version with vanishing isotropic-shift scaling factor and a CSA scaling factor of 0.39, but smaller CSA scaling factors are often required for $sp^2$-carbon spectra to fit into the spectral window of width $\omega_r$. For instance, a 200 ppm aromatic resonance at 100 Hz/ppm, scaled by 0.39, would extend over 7.8 kHz, and require a 10-kHz spectral window for the intensity to drop down to the baseline on both sides. Such high spinning speeds cannot be used with large rotors for several reasons, including mechanical limitations, finite pulse-length effects, and limited $^1$H decoupling power. In smaller rotors, the sensitivity is reduced. Also, with a typical 3-$\mu$s 90° pulse length, at 10-kHz spinning speed the four 180° pulses would extend over 25% of the 100-$\mu$s rotation period, which would lead to significant distortions due to interference of pulse and sample-rotation effects. Smaller scaling factors cannot be used for characterizing CSAs in samples with a wide range of isotropic shifts, since the signals that are off-resonance in $\omega_1$ will extend into the artifacts at the limits of the $\omega_1$ spectral width. In addition, for protonated carbons, in particular $CH_2$ groups, the sequence of Tycko *et al.* requires very high decoupling fields of $\gamma B_{1,H} = 3\gamma B_{1,C}$ during the 180° $^{13}$C pulses (*26*). Thus, the power requirements for proton decoupling are daunting (*19*).

In this paper, we introduce a pulse sequence derived from Tycko's experiment, but with 360° pulses instead of 180° pulses. This modification was inspired by the 360° pulse technique of Bax *et al.* (*16*), which, however, produces distorted spectra at scaling factors >0.1 and is difficult to implement at spinning speeds >4 kHz. The new technique, termed *s*eparation of *u*ndistorted *p*owder patterns by *e*ffortless *r*ecoupling (SUPER), is very insensitive to pulse-length errors, produces no significant artifacts, and works at standard power levels and spinning speeds. The error terms arising from finite pulse strength and incorrect pulse lengths are calculated using average-Hamiltonian theory. The SUPER NMR method is demonstrated on samples extending to the ends of the radiofrequency coil, in a 7-mm-diameter rotor at moderate decoupling powers ($\gamma B_1/2\pi < 80$ kHz). Standard spinning speeds, between 2.5 Hz and 5 kHz, are used. Applications to samples containing various $sp^2$- and $sp^3$-hybridized carbon sites are shown, including polyethylene with its very strong C–H and H–H dipolar couplings and only moderate CSA width. Elimination of aliasing in $\omega_1$ and generation of a quasi-static projection by a straightforward time-domain shearing transformation is demonstrated.

## THEORETICAL BACKGROUND

The pulse sequence for the 2D SUPER technique is shown in Fig. 1. In the following, we will focus on the evolution period $t_1 = Nt_r$, where each rotation period $t_r$ contains a pair of specifically timed pulses, each of total duration $2mt_{360}$, where $t_{360}$ is a 360° pulse length and usually $m = 1$.

*Description for $\omega_1 \gg \omega_r$.* We will consider this pulse sequence first in the limit of $\gamma B_{1,C} = \omega_1 \gg \omega_r$. If this condition is fulfilled, rotation of the rotor during a 360° pulse is negligible and the chemical shift during the pulse is averaged to zero. Due

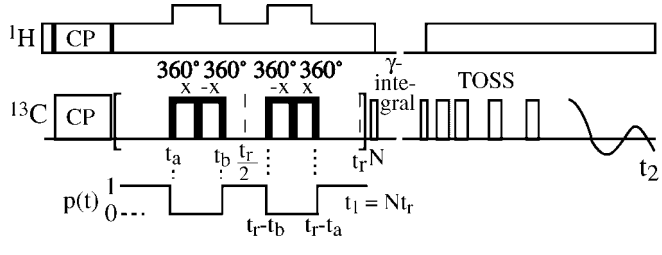


**FIG. 1.** Pulse sequence of the SUPER NMR experiment. The increment of the evolution time $t_1$ is one rotation period $t_r$. Each of the two pulse blocks in a given rotation period consists of two 360° pulses (or two 180° pulses flanking a 360° pulse; see Fig. 3). At the bottom of the figure, the function $p(t)$ multiplying the instantaneous frequency is shown; see text for more details. (It should not be confused with a trigger for rotor synchronization, which is not required in this experiment.)

to the resulting "gaps" in the CSA evolution, the CSA is not refocused into a rotational echo at the end of the rotation period; in other words, the CSA is recoupled. As in the experiment of Tycko *et al.* (*18*), the goal of the pulse sequence, based on the well-known time dependence of the CSA frequency under MAS (*1*),

$$\omega_{ani}(t) = C_1 \cos \omega_r t + C_2 \cos 2\omega_r t + S_1 \sin \omega_r t + S_2 \sin 2\omega_r t \quad [1]$$

$$\omega_r = 0\text{: static frequency } \omega_{ani,stat} = C_1 \cdot 1 + C_2 \cdot 1 + 0 = C_1 + C_2 \quad [2]$$

is to achieve an effective quasi-static anisotropic frequency

$$\bar{\omega}_{ani} = \frac{1}{t_r} \int_0^{t_r} p(t)\omega_{ani}(t)\, dt \stackrel{!}{=} \chi'(C_1 + C_2) = \chi' \omega_{ani,stat}. \quad [3]$$

Here $p(t) = 0$ during the pulses, i.e., for $t_a < t < t_b$ and $t_r - t_b < t < t_r - t_a$, and $p(t) = 1$ otherwise. The central condition in Eq. [3] can be fulfilled if the pulse timings (beginning $t_a$ and end $t_b$) are chosen such that

$$\frac{1}{t_r} \int_0^{t_r} p(t) \cos(\omega_r t)\, dt \stackrel{!}{=} \frac{1}{t_r} \int_0^{t_r} p(t) \cos(2\omega_r t)\, dt = \chi', \quad [4]$$

while the sine terms vanish for symmetry reasons. We can further calculate

$$\begin{aligned} \chi' &= \frac{1}{t_r} \int_0^{t_r} p(t) \cos(n\omega_r t)\, dt \\ &= \frac{1}{t_r} \int_0^{t_r} \cos(n\omega_r t) dt - 2\frac{1}{t_r} \int_{t_a}^{t_b} \cos(n\omega_r t)\, dt \\ &= -2\frac{1}{t_r} \int_{t_a}^{t_b} \cos(n\omega_r t)\, dt \\ &= \frac{1}{\pi n}(\sin(n\omega_r t_a) - \sin(n\omega_r t_b)) \quad (n = 1, 2). \end{aligned} \quad [5]$$

Comparison with Eq. [3] of ref. (*18*) shows that the central condition in Eq. [4] is fulfilled if the beginning $t_a$ and end $t_b$ of the 360° pulses are the times $T_1$ and $T_2$, respectively, of the $\delta$ function 180° pulses in an idealized Tycko experiment (*18*). The scaling factor $\chi'$ is half of the corresponding scaling factor $\chi$ in the experiment of Tycko *et al.* The $t_a/t_r$ and $t_b/t_r$ values that fulfill Eq. [5] and the $t_a$ dependence of $\chi'$ are plotted in Fig. 2. The following simple polynomial approximations enable easy determination of any valid combination of start and end

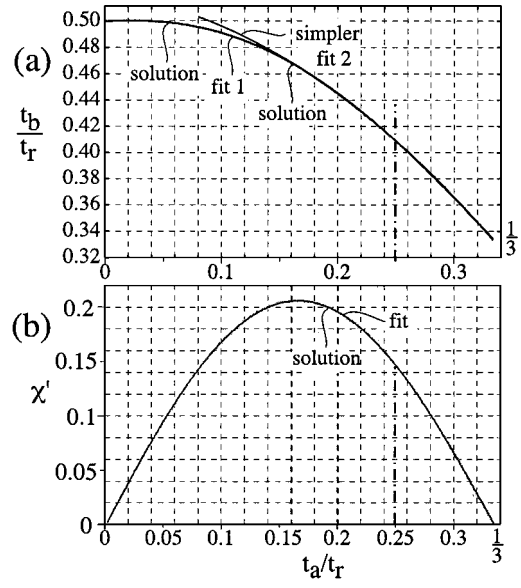


**FIG. 2.** (a) Pulse-termination time $t_b/t_r$ and (b) scaling factor $\chi'$ plotted as a function of the pulse-initiation time $t_a/t_r$. Polynomial fits with coefficients given in the text are also shown. Over wide ranges, the original curves and the polynomial fits are virtually indistinguishable. Two different fits are shown for $t_b/t_r$, as described in the text. The dashed-dotted line at $t_a/t_r = 0.25$ marks the pulse timings chosen for the experimental spectra shown below, with $\chi' = 0.15(5)$.

times $t_a$ and $t_b$ of the pulses, and of the corresponding scaling factor $\chi'$:

$$t_b(t_a) = t_r\{0.4994 + 0.057(t_a/t_r) - 1.0332(t_a/t_r)^2 - 4.7533(t_a/t_r)^3 + 8.6362(t_a/t_r)^4\} \quad \text{for } 0 < t_a < t_r/3. \quad [6a]$$

$$t_b(t_a) = t_r\{0.5195 - 0.0958(t_a/t_r) - 1.3917(t_a/t_r)^2\} \quad \text{for } t_r/6 < t_a < t_r/3. \quad [6b]$$

$$\chi'(t_a) = -0.0006 + 2.0526(t_a/t_r) - 0.7196(t_a/t_r)^2 - 33.6982(t_a/t_r)^3 + 52.2845(t_a/t_r)^4. \quad [6c]$$

The simpler approximation of Eq. [6b] works well in the $t_a$ range that is experimentally relevant. The $\chi'(t_a)$ curve is approximately symmetric with respect to $t_r/6$.

Taking into account also the isotropic chemical shift (combined with the radiofrequency offset term), the overall effective frequency and the isotropic-shift scaling factor $\xi'$ during the recoupled evolution period are given by

$$\bar{\omega} = \bar{\omega}_{ani} + \omega_{iso} \frac{1}{t_r} \int_0^{t_r} p(t)\, dt = \chi' \omega_{ani,stat} + \xi' \omega_{iso} \quad [7a]$$

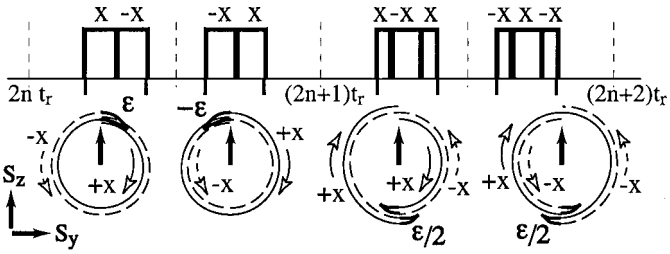


**FIG. 3.** Schematic representation of the CSA average-Hamiltonian calculation for the SUPER experiment in the presence of pulse-length errors.

with

$$\xi' = \frac{1}{t_r}\int_0^{t_r} p(t)\,dt = 1 - 2\frac{t_b - t_a}{t_r}. \qquad [7b]$$

*Compensation of pulse-length errors.* The sequence of Fig. 1 lends itself to good compensation of $B_1$ inhomogeneities, or equivalently pulse-length errors. Most importantly, the forward and matching backward nutation takes the toggling-frame Hamiltonian back to $z$ for the windows between the pulses, regardless of the pulse strength.

As shown in Fig. 3, a pulse-length error in the $(x, -x)$ pulse pair leads to uncompensated $S_z$ and $S_y$ components in the average Hamiltonian,

$$\bar{H}_{CSA}^{\text{pulerr}} \approx \frac{2}{\omega_1 t_r}\omega(\pm t_{ab})\int_0^{\varepsilon}\{S_z\cos\omega_1 t \pm S_y \sin\omega_1 t\}\,d\omega_1 t$$
$$= \frac{2}{\omega_1 t_r}\omega(\pm t_{ab})\{S_z\sin\varepsilon \pm S_y(1-\cos\varepsilon)\}, \qquad [8]$$

where $\pm S_y$ results from $\pm x$ pulses, while $\pm t_{ab} = \pm(t_a + t_b)/2$ is the center of either pulse pair. For the isotropic shift and the $C_n$ components of $\omega(\pm t_{ab})$, the $y$ components of the error terms of the two pulse pairs in a rotation period cancel. For the $S_n$ terms of $\omega(\pm t_{ab})$, small $y$ components remain, but they will be truncated to zero by the dominant $z$ Hamiltonian $\chi'(C_1 + C_2)S_z$.

The $z$ error can be significantly reduced by applying two 180°–360°–180° pulses in every other rotation period; see Fig. 3. The average pulse-length error Hamiltonian for these pulses is

$$\bar{H}_{CSA}^{\text{pulerr}} = \frac{2}{\omega_1 t_r}\{\omega(\pm t_{ab} - t_{180}) + \omega(\pm t_{ab} + t_{180})\}$$
$$\times \int_{\pi}^{\pi+\varepsilon/2} S_z\cos\omega_1 t\,d\omega_1 t$$
$$\approx \frac{-4}{\omega_1 t_r}\omega(\pm t_{ab})S_z\sin\{\varepsilon/2\}. \qquad [9]$$

The sign of this $z$ component is opposite to that in Eq. [8]. The average pulse-error Hamiltonian after two rotation periods is approximately

$$\bar{H}_{CSA,z}^{\text{pulerr,2tr}} \approx \frac{2}{\omega_1 t_r}(\omega(t_{ab}) + \omega(-t_{ab}))S_z\frac{1}{2}(\sin\varepsilon - 2\sin\{\varepsilon/2\})$$
$$= \frac{1}{\omega_1 t_r}2(C_1\cos\omega_r t_{ab} + C_2\cos 2\omega_r t_{ab})$$
$$\times S_z(\sin\varepsilon - 2\sin\{\varepsilon/2\})$$
$$\approx (C_1 + C_2)S_z\frac{1}{2}\frac{(-1)}{4\omega_1 t_r}\varepsilon^3. \qquad [10]$$

In the last step, we used that $\omega_r t_{ab} \simeq 2\pi/3$. According to these approximations, the error term is negligible for $\varepsilon \le \pi/6$ and still small for $\varepsilon \le \pi/2$ (i.e., a $B_1$-field strength deviation of ±25%). In addition, being proportional to $(C_1 + C_2)S_z$, it will not distort the lineshape seriously, but just modify the scaling factor slightly. Generally, it should be noted that signals from spins near the ends of the coil are significantly suppressed by the reduced efficiencies of $^1$H pulse excitation, cross polarization, and detection.

The 64-step phase sequence used to obtain the experimental spectra shown below is given in Table 1. In the pulse program, four phase lists $\phi_1$ through $\phi_4$ are used, which can all be derived from that given in the table by simple sign changes, as explained in the note to the table and depicted in Fig. 3.

*Finite pulse-strength effects.* For an accurate calculation of the average Hamiltonian of the SUPER evolution, we need to consider that the sample rotation changes the anisotropic

**TABLE 1**
**Sixty-Four-Phase Sequence Used for the Pulses in the SUPER NMR Evolution Period**

| $\phi_a$ | $\phi_b$ | $\phi_a$ | $\phi_b$ | $\phi_a$ | $\phi_b$ | $\phi_a$ | $\phi_b$ | $\phi_a$ | $\phi_b$ | $\phi_a$ | $\phi_b$ | $\phi_a$ | $\phi_b$ | $\phi_a$ | $\phi_b$ |
|---|---|---|---|---|---|---|---|---|---|---|---|---|---|---|---|
| $+x$ | $-x$ | $+y$ | $-y$ | $-x$ | $+x$ | $-y$ | $+y$ | $+x$ | $+x$ | $+y$ | $+y$ | $-x$ | $-x$ | $-y$ | $-y$ |
| $-x$ | $+y$ | $-x$ | $-y$ | $+x$ | $-y$ | $+x$ | $+y$ | $+x$ | $+y$ | $-x$ | $+y$ | $-x$ | $-y$ | $+x$ | $-y$ |
| $-y$ | $-x$ | $+y$ | $-x$ | $-y$ | $+x$ | $-y$ | $+x$ | $+y$ | $+x$ | $+y$ | $-x$ | $+y$ | $-x$ | $-y$ | $+x$ |
| $-y$ | $+x$ | $-x$ | $+y$ | $-y$ | $-x$ | $+x$ | $-y$ | $+y$ | $+x$ | $+x$ | $+y$ | $+y$ | $-x$ | $-x$ | $-y$ |

*Note.* The 180° pulse phases in two successive rotation periods are $(\phi_a, \phi_a, -\phi_a, -\phi_a)$, $(-\phi_a, -\phi_a, \phi_a, \phi_a)$, $(\phi_b, -\phi_b, -\phi_b, \phi_b)$, and $(-\phi_b, \phi_b, \phi_b, -\phi_b)$. The phases listed in the table are $(\phi_a, \phi_b, \phi_a, \phi_b, \ldots)$, to be read row by row. In a typical pulse program, the phases of the two blocks of pulses in each rotation period are encoded most conveniently using four phase programs, $(\phi_1, \phi_2, \phi_3 = -\phi_1, \phi_4 = -\phi_2)$ and $(\phi_3, \phi_4, \phi_1, \phi_2)$. Here, $\phi_1$ is the phase list given in the table $(\phi_a, \phi_b)$, starting as $(+x, -x, +y, -y, \ldots)$, while $\phi_2$ is obtained from that phase list by alternating the signs of the entries $(\phi_a, -\phi_b)$, i.e., starting as $(+x, +x, +y, +y, \ldots)$. The other two phase lists are obtained as $\phi_3 = -\phi_1$ and $\phi_4 = -\phi_2$.

chemical shift during a 360° pulse. As a result, the CSA is not averaged exactly to zero during the pulse. Instead, the average Hamiltonian during the first of the two contiguous pulse pairs is given by

$$\bar{H}_{CSA}^{pulse} = \frac{1}{t_r}\int_{t_a}^{t_b} \omega(t)\{S_z \cos\omega_1(t-t_a) + S_y \sin\omega_1(t-t_a)\}\,dt, \qquad [11]$$

where $S_x$ and $S_y$ are the transverse components of the spin operator of the $^{13}$C nuclear spins. Note that the sign of $\omega_1$ changes when the phase of the pulse is inverted, and that as for the average frequency in Eq. [3], the average is calculated per rotation period. For the second 360° pulse pair in the rotation period, an analogous expression, of equal magnitude, has to be evaluated. In order to analyze Eq. [11], the integrals for the four terms of $\omega(t)$ in Eq. [1] are calculated separately, and the average for both pulse pairs in a rotation period is calculated. The factors in front of $S_yC_n$ and $S_zS_n$, $n = 1$ and 2, are zero after a full rotation period for symmetry reasons. The factors multiplying $S_zC_n$ are

$$\begin{aligned} f_{z,C_n} &= \frac{2}{t_r}\int_{t_a}^{t_b} \cos n\omega_r t \cos(\omega_1(t-t_a))\,dt \\ &= \frac{2n\omega_r/t_r}{\omega_1^2 - (n\omega_r)^2}[\sin n\omega_r t_a - \sin n\omega_r t_b] \\ &= \frac{(n(t_b-t_a)/t_r)^2}{4-(n(t_b-t_a)/t_r)^2}\chi', \end{aligned} \qquad [12]$$

where we have used $\omega_1 = 4\pi/(t_b - t_a)$ and Eq. [5]. The term $S_z(C_1 + C_2)1/2(f_{z,C1} + f_{z,C2})$ only modifies the scaling factor, while $S_z(C_1 - C_2)1/2(f_{z,C1} - f_{z,C2})$ is the error term that produces potentially the most serious lineshape distortions. Due to the small numerator in the last line of Eq. [12], in the relevant range of $t_a$ these terms remain almost negligible; see Fig. 4a. For instance, at $t_a = 0.25\ t_r$, the scaling factor $\chi'$ is increased only by 3%, from 0.15 to 0.155, and the other $z$ error is even smaller.

The $S_y$ error components

$$\begin{aligned} f_{y,S_n} &= \frac{2}{t_r}\left(\int_{t_a}^{t_{ab}} \sin n\omega_r t \sin\{\omega_1(t-t_a)\}\,dt \right. \\ &\quad \left. - \int_{t_{ab}}^{t_b} \sin n\omega_r t \sin\{\omega_1(t-t_{ab})\}\,dt\right) \\ &= \frac{2\omega_1/t_r}{\omega_1^2 - (n\omega_r)^2}(\sin\{n\omega_r t_a\} + \sin\{n\omega_r t_b\} \\ &\quad - 2\sin\{n\omega_r(t_a+t_b)/2\}) \end{aligned} \qquad [13]$$

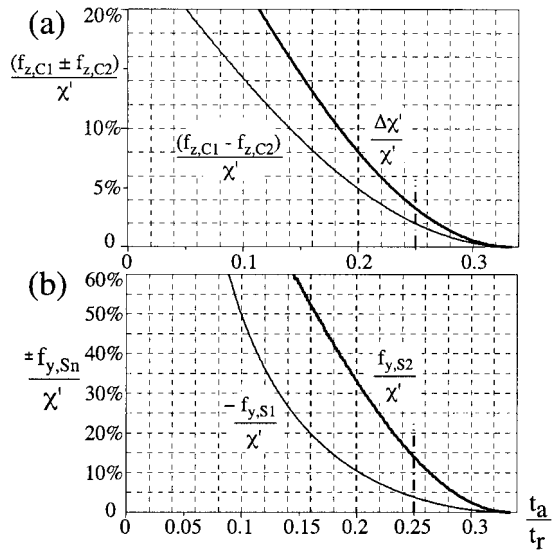


**FIG. 4.** Plot of the residual CSA average-Hamiltonian error terms, in % of the desired scaling factor $\chi'$, during pulses in one rotation period as a function of the pulse-initiation time $t_a/t_r$. (a) $S_z$ terms $1/2(f_{z,C1}+f_{z,C2})/\chi' = \Delta\chi'/\chi'$ and $1/2(f_{z,C1} - f_{z,C2})/\chi'$. (b) $S_y$ terms $-f_{y,S1}/\chi'$ and $f_{y,S2}/\chi'$; the former term is plotted with a negative sign for ease of comparison. Within the $t_a/t_r$ range of interest ($t_a/t_r \geq 0.2$), the $z$ error terms in (a) are only a few percent of $\chi'$. However, the $y$ errors in (b) become significant as $t_a/t_r$ decreases (due to the concomitant decrease in $B_1$ field strength). The dashed-dotted line marks the pulse timings chosen for the experimental spectra shown below, with $\chi' = 0.155$.

are nearly an order of magnitude larger; see Fig. 4b. However, if $(S_1 f_{y,S1} + S_2 f_{y,S2})S_y$ can be kept at <20% of the $z$ term $\chi'(C_1 + C_2)S_z$, it will be truncated to zero by that large orthogonal $z$ Hamiltonian. The $y$ terms can also be reduced by the phase sequence of the pulses in successive rotation periods; see Table 1. Figure 4 shows plots of the error terms $1/2(f_{z,C1} + f_{z,C2})/\chi'$, $1/2(f_{z,C1} - f_{z,C2})/\chi' = \Delta\chi'/\chi'$, $f_{y,S1}/\chi'$, and $f_{y,S2}/\chi'$ as a function of $t_a/t_r$. The $y$ error terms are probably the reason that the version of the experiment with $t_a/t_r = 0.19$, $\omega_1/\omega_r = 8$, and a larger scaling factor $\chi' = 0.2$ shows significant oscillatory distortions of the powder pattern, while the version with $t_a/t_r = 0.25$, $\omega_1/\omega_r = 12$, and $\chi' = 0.15$ works well. The use of stronger pulses of 4 $t_{360}$ (rather than 2 $t_{360}$) duration per block should result in improved behavior for the versions with the largest scaling factors.

Artifacts are suppressed successfully by making the pulse phases in the sequence nonperiodic; see Table 1. Note that the isotropic-shift scaling factor $\xi'$ is not changed by the effects discussed in this section, since the isotropic chemical shift is unaffected by the sample rotation.

*Heteronuclear decoupling.* Exact $^{13}$C 360° pulses decouple the $^{13}$C–$^{1}$H dipolar interaction. Thus, ideally no proton irradiation is required during the $^{13}$C 360° pulses in the SUPER pulse sequence. For unprotonated carbons with large CSAs, $^{1}$H decoupling during the $^{13}$C 360° pulses is indeed dispensable. However, even with small deviations of the pulse flip angle from

360°, or with a tilted effective field due to $^{13}$C chemical-shift offset, the strong heteronuclear coupling will dephase the signal of protonated carbons. Therefore, irradiation on the proton channel during the carbon pulses is desirable. However, the $B_{1,H}$ field strength has to be chosen appropriately to avoid a strong non-vanishing average dipolar Hamiltonian. The average heteronuclear dipolar Hamiltonian of a $^{13}$C 360° $x$ pulse is

$$\bar{H}_{IS}^{2\pi\,pulse} \approx 2\omega_{IS}\frac{1}{2\pi}\int_0^{2\pi}\{I_z\cos(k\omega_{1C}t) + I_y\sin(k\omega_{1C}t)\} \times \{S_z\cos\omega_{1C}t + S_y\sin\omega_{1C}t\}d(\omega_{1C}t), \quad [14]$$

where $k = \gamma_H B_{1,H}/\gamma_C B_{1,C}$. The small effects of sample rotation on $\omega_{IS}$ during the pulse have been neglected here. The average Hamiltonian of Eq. [14] vanishes and good decoupling is achieved for

$$k = 2 = \omega_{1,H}/\omega_{1,C}. \quad [15]$$

Under this condition Eq. [15], Eq. [14] applies even for a $^{13}$C 360° pulse that has been split into 180° pulses, since the 360° rotation of the $^1$H term is completed within one 180° pulse, and the average Hamiltonian is unaffected by changes in the sequence of its component terms. For the $\chi' = 0.15$ scaling factor used throughout this work, $\omega_{1,C} = 12.12\,\omega_r$ and $\omega_{1,H} = 25\,\omega_r$ according to Eq. [15]. In practice, we observed good decoupling at the slightly stronger $\omega_{1,H} = 30\,\omega_r$. Thus, $\omega_{1,H} = 75$ kHz can be used for $\omega_r = 2.5$ kHz, or $\omega_{1,H} = 120$ kHz with $\omega_r = 4$ kHz. For protonated olefinic and aromatic carbons with their large CSAs, we have obtained satisfactory powder spectra for $\omega_{1,H}/\omega_{1,C} = 1.6$.

*Shearing of spectra.* According to Eq. [7], the frequency in $\omega_1$ is not only the scaled anisotropic chemical shift, but also includes a slightly scaled isotropic chemical shift (combined with the frequency offset). With radiofrequency irradiation near $\omega_{iso}$ of the peak of interest, the scaled CSA spectrum will sit in the middle of the $\omega_1$ spectral range of width $\omega_r$. However, if the isotropic chemical shifts cover a wide range of frequencies, the (scaled) isotropic shift will result in some of the powder patterns being aliased, i.e., appearing at the other end of the $\omega_1$ spectral range. An example is shown in Fig. 5a. Since all the necessary spectral components are present and no artifacts are detected in the spectral patterns, the full powder spectra can nevertheless be reconstructed. The conceptually simplest procedure would be to replicate the 2D spectrum several times in $\omega_1$ and then shear it parallel to $\omega_1$ (in the frequency domain). However, this procedure generates a bloated (intermediate) data matrix, and the shearing angle may be restricted to specific values due to the discrete nature of the data matrix.

Continuous shearing (*16*) is easily achieved during data processing based on the following well-established principles: After Fourier transformation over $t_2$ and phasing in $\omega_2$, the real parts

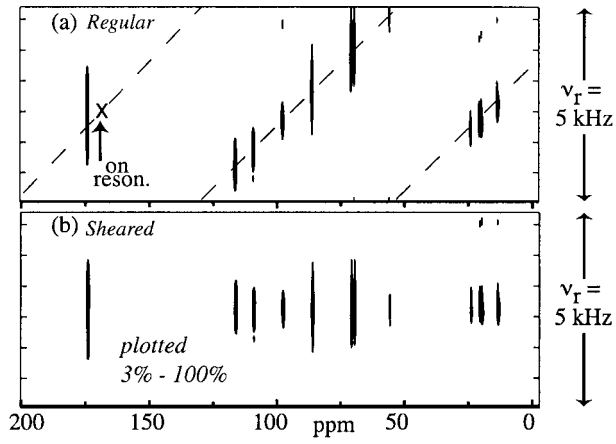


**FIG. 5.** (a) Unsheared 2D SUPER spectrum of (-)-2,3:4,6-di-*O*-isopropylidene-2-keto-L-gulonic acid, taken at $\omega_r/2\pi = 5$ kHz. The diagonal of the spectrum, which is aliased several times, is plotted as a dashed line. The on-resonance position is marked by an "x". (b) The same data after shearing that removes the isotropic shift in $\omega_1$. Twenty contour lines are plotted with linear increments between 3 and 100% of the maximum intensity. No significant artifacts are visible in the spectra, except for low "wings" of the protonated-carbon sites, e.g., near 70 ppm, which are due to residual C–H dipolar broadening, resulting from the $^1$H decoupling power during the $^{13}$C pulses being too low ($\gamma B_{1,H}/2\pi = 30$ kHz).

of the sine and cosine signals of a specific site are

$$\langle\cos(\bar{\omega}t_1)\rangle\delta(\omega_2 - \omega_{iso}) \quad \text{and} \quad \langle\sin(\bar{\omega}t_1)\rangle\delta(\omega_2 - \omega_{iso}) \quad [16]$$

with $\bar{\omega}$ given by Eq. [7]. The angle brackets indicate the powder average over all orientations. The two signal components can be combined in the standard way to give a complex exponential in $t_1$

$$\begin{aligned} s(t_1, \omega_2) &= \langle\cos(\bar{\omega}t_1) + i\sin(\bar{\omega}t_1)\rangle\delta(\omega_2 - \omega_{iso}) \\ &= \langle\exp(i\bar{\omega}t_1)\rangle\delta(\omega_2 - \omega_{iso}) \\ &= \exp(i\xi'\omega_{iso}t_1)\langle\exp(i\bar{\omega}_{ani}t_1)\rangle\delta(\omega_2 - \omega_{iso}) \\ &= \exp(i\xi'\omega_2 t_1)\langle\exp(i\bar{\omega}_{ani}t_1)\rangle\delta(\omega_2 - \omega_{iso}). \end{aligned} \quad [17]$$

In the last step, the properties of the $\delta$ function were used. In order to make it permissible to approximate the MAS peak in $\omega_2$ by a delta function, line broadening in $\omega_2$ should be applied (by convolution) only *after* the final 2D spectrum has been obtained. By multiplying the signal of Eq. [17] with a phasing factor proportional to $\omega_2$ and $t_1$, we can remove the isotropic-shift effect from the first dimension:

$$\begin{aligned} s'(t_1, \omega_2) &= \exp(-i\xi'\omega_2 t_1)s(t_1, \omega_2) \\ &= \langle\exp(i\bar{\omega}_{ani}t_1)\rangle\delta(\omega_2 - \omega_{iso}). \end{aligned} \quad [18]$$

After FT over $t_1$, this gives a 2D spectrum with a pure-anisotropy

$\omega_1$ dimension:

$$\mathrm{Re}(S'(\omega_1, \omega_2)) = \langle \delta(\omega_1 - \bar{\omega}_{ani}) \rangle \delta(\omega_2 - \omega_{iso}). \quad [19]$$

Figure 5b shows the result of this shearing procedure, using the theoretical chemical-shift scaling factor $\xi'$, which is 0.667. The data were also phased by multiplying the complex $S'(\omega_1, \omega_2)$ with $\exp(ic\omega_2)$, where the constant $c$ was determined so as to yield all-positive signals. Even though this appears to be a linear phase correction in $\omega_2$, it is in effect a linear phase correction in $\omega_1$, since only the $\omega_1$ dimension has retained its dispersive part.

In the most reliable procedure for CSA determination, the principal values from the SUPER spectrum should be used as starting values in a best-fit simulation of the spectrum without sample spinning. For this purpose, it is very useful to shear the 2D SUPER spectrum partially so that the residual isotropic-shift scaling factor in $\omega_1$ equals the anisotropy scaling factor $\chi'$. Then, the projection onto the $\omega_1$ axis will look like the static 1D spectrum, and the features in that spectrum can be assigned to specific powder patterns. The partial shearing is achieved by reducing the shearing factor in Eq. [18] from $\xi'$ to $\xi'' = \xi' - \chi'$:

$$\begin{aligned} s''(t_1, \omega_2) &= \exp(-i\xi''\omega_2 t_1) s(t_1, \omega_2) \\ &= \langle \exp(i(\chi'(\omega_{iso} + \omega_{ani})t_1)) \rangle \delta(\omega_2 - \omega_{iso}). \end{aligned} \quad [20]$$

An example of the usefulness of this partial-shearing procedure is shown in Fig. 11 below. The data processing described in this section was performed on a PowerMac using the Matlab (MathWorks, Natick, Massachusetts) software.

## RESULTS AND DISCUSSIONS

*SUPER spectra of COO carbons.* Figure 6 shows various COO chemical-shift patterns measured by the SUPER technique for $^{13}$C-labeled and unlabeled molecular crystals and amorphous polymers. Typical quasi-static powder patterns have been obtained. These patterns were measured with very weak $^1$H decoupling during the $^{13}$C pulses, at a spinning speed of 5 kHz. For the compounds of Figs. 6b and 6f, the comparison with the static powder patterns shown in Refs. (*27–29*) confirms the reliability of the SUPER method. The principal values obtained here and reported in the literature are compared in Table 2. The variation is ±3 ppm or less; this is typical of the deviations between CSA results from different MAS experiments.

For some chemical groups with similar isotropic-shift ranges, systematic differences in CSAs have been reported in the literature (*8*). For example, the chemical-shift lineshapes of COOC ester groups are systematically different from those of most other COO or of CON groups. The COOC groups have small asymmetry parameters $\eta$ and positive anisotropy parameters $\delta$; in other words, the $\sigma_{22}$ peak occurs at low ppm values (about 134 ppm). This can be used to assign resonances to COOC groups. At the bottom of Fig. 6, typical powder patterns, based on average principal values in the literature (*8*), are displayed for carboxylate, carboxylic acid, and ester groups. In the right column of Fig. 6, SUPER CSA spectra of COOC esters are shown, and in the left column, of $COO^-$ and COOH groups. Note in particular that the COO group of PEMA, Fig. 6f, with a very downfield isotropic chemical shift of 177 ppm, in a region typical of $COO^-$, is recognized as an ester group based on its CSA lineshape. The COOH and COOC groups in fumaric acid monoethyl ester, Figs. 6c and 6d, can be assigned immediately based on the characteristic COOH and COOC CSA lineshapes.

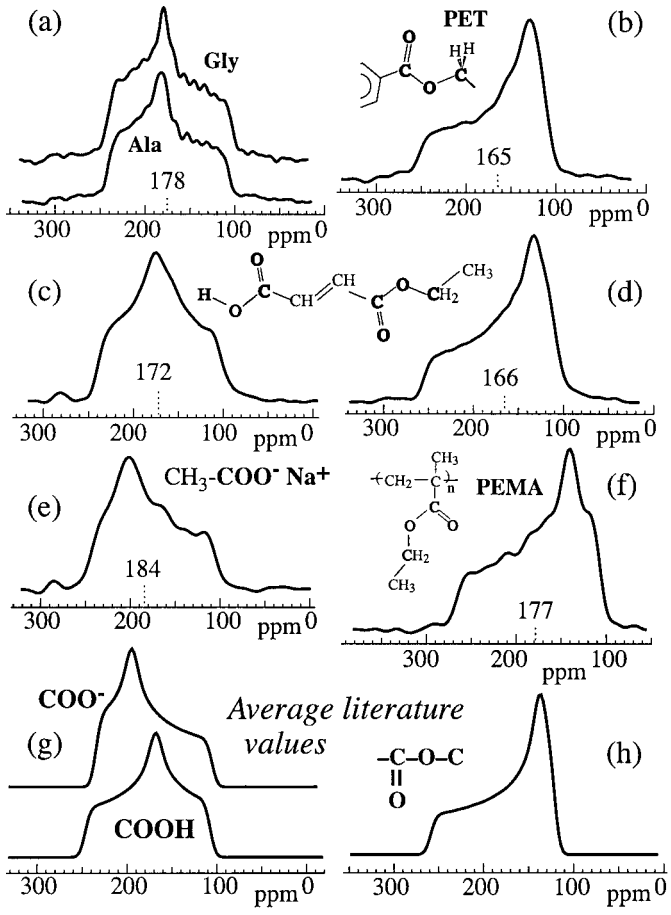


**FIG. 6.** COO powder spectra obtained as cross sections from 2D SUPER of (a) glycine and alanine ($^{13}$COO-labeled); (b) 10% $^{13}$COO-labeled PET; (c, d) acid and ester sites, respectively, of fumaric acid monoethyl ester; (e) sodium acetate; and (f) 20% $^{13}$COO-labeled PEMA ($\omega_{iso} = 177$ ppm). These spectra were taken at $\omega_r/2\pi = 5$ kHz, with $\chi' = 0.155$ like all other spectra in this work, with weak $^1$H decoupling power ($\gamma B_{1,\mathrm{H}}/2\pi = 30$ kHz) during the $^{13}$C pulses. No shearing was used in the processing. The maximum $t_1$ was between 16 and 32 $t_r$. The ppm scales, which show quasi-static chemical shifts $\omega/\chi'$, were shifted to match the isotropic chemical shifts correctly; these are given for each spectrum above the short vertical dashed line. The scales are shifted relative to each other due to the different isotropic shifts and because slightly different offsets were used in the various experiments. (g, h) Simulated powder patterns obtained with the average principal values given in Ref. (*8*) for (g) carboxylate and carboxylic acid groups and (h) ester groups.

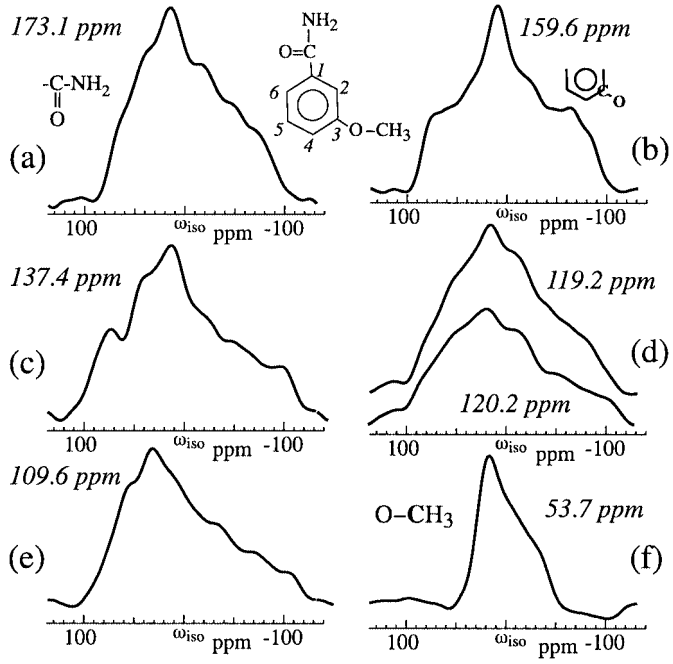


**FIG. 7.** Cross sections from the 2D SUPER spectrum of 3-methoxy benzamide (*m*-anisamide), taken at $\omega_r/2\pi = 4$ kHz, at the indicated ppm values in the MAS spectrum. The 2D SUPER spectrum was sheared to move the isotropic shift to $\omega_1 = 0$ ppm.

*SUPER spectrum of 3-methoxy benzamide.* Figure 7 shows six powder patterns from the sheared SUPER spectrum of 3-methoxy benzamide. The powder pattern of the C=O resonance at 173.1 ppm, Fig. 7a, clearly excludes an ester functionality. In addition, its large width $\sigma_{33} - \sigma_{11}$ indicates the amide structure (*8*). The aromatic ether at 159.6 ppm shows a nice powder pattern, Fig. 7b. Other aromatic sites, Figs. 7c–7e, exhibit recognizable powder patterns, all with the $\sigma_{22}$ peak downfield from the isotropic shift (center of gravity), as is typical for aromatics. The assignment of the aromatic signals given in Table 2 is based on dipolar dephasing, empirical chemical-shift prediction, and $^1$H–$^{13}$C long-range correlations. The $OCH_3$ group, Fig. 7f, shows the much narrower powder pattern typical of an $sp^3$-hybridized carbon. The spectrum was obtained at $\nu_r = 4$ kHz with moderate $\gamma B_{1,H}/2\pi = 76$ kHz proton decoupling. This is below the optimum decoupling power level of $25 * \nu_r = 100$ kHz (see above), so with higher $^1$H decoupling power, the resolution could be increased.

*SUPER spectra of aromatic and olefinic carbons.* Similarly as between COOC and other COO/CON sites, a CSA-based distinction is possible between aromatic rings and olefinic C=C carbons[8]. Again, the position of the $\sigma_{22}$ peak is characteristically different. As examples, Fig. 8 shows SUPER spectra of the olefinic H–C=C–H sites in fumaric acid monoethyl ester, of aromatic carbons in polystyrene, and of the mobile phenylene rings in bisphenol-A polycarbonate, obtained under the same conditions as the spectrum of Fig. 7. In the crystalline fumaric acid monoethyl ester, segmental motions are of small amplitude and uniform, so nearly ideal powder spectra of the olefinic carbons are obtained, Fig. 8a, which can easily be simulated, Fig. 8b. The difference in the $\sigma_{22}$ peak positions of the olefinic carbons in Fig. 8a and of the aromatic carbons in Figs. 7b–7e is clearly visible.

In the spectrum of amorphous polystyrene (PS), Fig. 8c, the steps at the end of the spectrum of the aromatic CH groups are lower than in a simple powder pattern. These distortions can be reproduced at least qualitatively using a model that assumes motions around the bond connecting the phenyl ring to the polymer backbone, Fig. 8d. The amplitudes of the motions of the rings in the various environments in this glassy polymer are assumed to be described by a Gaussian distribution centered on 0°, with a

**TABLE 2**

**Chemical-Shift Principal Values and Isotropic Chemical Shifts, in ppm from Tetramethyl Silane (with the Lines of Adamantane as an External Secondary Reference, at 38.5 and 29.5 ppm), of $sp^2$-Carbons and a Methoxyl Group in the Compounds Studied Here by the SUPER NMR Technique**

| Compound name/carbon site | $\sigma_{11}$ (ppm) | $\sigma_{22}$ (ppm) | $\sigma_{33}$ (ppm) | $\sigma_{iso}$ (ppm) |
|---|---|---|---|---|
| Glycine | 244 | 181 | 104 | 176.4 |
| **Glycine literature** | **247** | **182** | **103** | **177** |
| L-Alanine | 242 | 184 | 108 | 177.9 |
| **l-Alanine literature** | **243** | **184** | **107** | **178** |
| Poly(ethylene terephthalate) (PET) | 250 | 130 | 115 | 165.3 |
| **PET literature** | **252** | **126** | **113** | **164** |
| Poly(ethyl methacrylate) (PEMA) | 271 | 147 | 115 | 177.7 |
| **PEMA literature** | **268** | **150** | **113** | **177** |
| Sodium acetate | 244 | 202 | 104 | 183.6 |
| (-)-2,3:4,6-Di-*O*-isopropylidene-2-keto-L-gulonic acid | 252 | 157 | 105 | 171.6 |
| Fumaric acid monoethyl ester (*COOH) | 239 | 176 | 102 | 172.1 |
| Fumaric acid monoethyl ester (*COOC) | 257 | 131 | 110 | 166.1 |
| *m*-Anisamide CO–$NH_2$ | 248 | 188 | 83 | 173.1 |
| *m*-Anisamide ring carbon 1 | 230 | 150 | 31 | 137.4 |
| *m*-Anisamide ring carbon 2 | 188 | 142 | 0 | 109.6 |
| *m*-Anisamide ring carbon 3 | 242 | 170 | 68 | 159.6 |
| *m*-Anisamide ring carbon 4 (or 6) | 197 | 137 | 23 | 119.2 |
| *m*-Anisamide ring carbon 5 | 218 | 159 | 14 | 130.2 |
| *m*-Anisamide ring carbon 6 (or 4) | 200 | 141 | 11 | 120.2 |
| *m*-Anisamide $OCH_3$ | 78 | 72 | 12 | 53.7 |
| Fumaric acid m. ester ($R_1$*CH=$CHR_2$) | 245 | 119 | 44 | 136.6 |
| Fumaric acid m. ester ($R_1$CH=*$CHR_2$) | 230 | 123 | 50 | 134.0 |
| Polystyrene (PS) quaternary C | 233 | 186 | 19 | 146 |
| Polystyrene (PS) aromatic CH | 225 | 132 | 28 | 128 |
| Polycarbonate (PC) aromatic CH | 193 | 164 | 27 | 127.8 |
| Polycarbonate (PC) aromatic CH | 174 | 149 | 38 | 120.5 |

*Note.* The anisotropy scaling factor was $\chi' = 0.155$, which contains a 3% correction by the $\Delta\chi'/\chi'$ contribution to the average Hamiltonian as plotted in Fig. 4a. Where available, chemical-shift literature values from Ref. (*8*) are given for comparison. The isotropic shifts were obtained from magic-angle spinning. The principal values were rounded to the nearest ppm and therefore their average is not exactly equal to the isotropic shift. The error margins for the principal values of the unprotonated carbons are ±3 ppm, and for the protonated aromatic carbons, ±5 ppm.

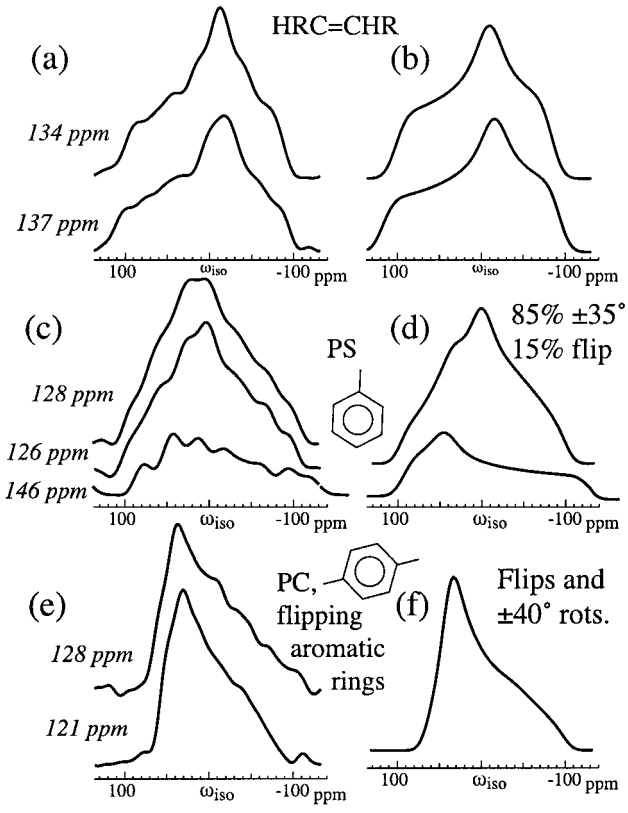


**FIG. 8.** Distinction of olefinic vs aromatic $sp^2$-hybridized carbon sites based on their chemical-shift principal values. Cross sections from 2D SUPER spectra are shown, sheared to move the isotropic shift to $\omega_1 = 0$ ppm. Spectra taken at $\omega_r/2\pi = 4$ kHz. (a) H–C=C–H carbons of fumaric acid monoethyl ester. (b) Corresponding simulated powder pattern (with CSA principal values given in Table 2). (c) Aromatic carbons of polystyrene. Two protonated-carbon cross sections and the signal of the unprotonated carbons are shown. (d) Corresponding simulations. A distribution of ring libration amplitudes of 35° standard deviation, as well as a fraction of 15% of flipping rings, was included in the simulation for the protonated carbons. (e) Protonated aromatic carbons in bisphenol-A polycarbonate. (f) Simulation of the PC spectra, assuming ring flips and a distribution of ring-libration amplitudes with a standard deviation of 40°.

standard deviation $\sigma = 35°$. Such medium-amplitude motions of the rings have also been deduced from C–H dipolar and $^2$H quadrupolar spectra (*30, 31*). In addition, a minor fraction (15% in our simulated spectrum) of the rings in PS also undergoes 180° flips, giving rise in particular to a peak to the left of the central maximum.

The spectra of the protonated aromatic sites of bisphenol-A polycarbonate, Fig. 8d, also show indications of a broad distribution of small- and medium-amplitude motions. Again, it is known from $^2$H quadrupolar and C–H dipolar spectra that all rings flip on the 100-$\mu$s timescale at ambient temperature, and that the rings undergo medium-amplitude motions (*31, 32*). The simulation of Fig. 8f uses a Gaussian distribution of wobbling amplitudes centered on 0° with a standard deviation $\sigma = 40°$.

*SUPER spectra of aliphatic carbons.* SUPER powder patterns of aliphatic carbons are shown in Figs. 9–11. The data were recorded at $\omega_r/2\pi = 2.5$ kHz, with $\gamma B_{1,H}/2\pi = 75$ kHz proton decoupling. This fulfills the condition of $\omega_{1,H}/\omega_{1,C} > 2$ and thus provides good heteronuclear decoupling.

Figure 9 shows SUPER cross sections for high-density polyethylene, which is particularly challenging due to its large H–C and H–H dipolar couplings. The crystalline resonance in Fig. 9a shows the powder pattern of near-rigid polyethylene, with principal values in good agreement with the literature (*33, 34*). The corresponding simulation is shown in Fig. 9b. A cross section taken between the crystalline and amorphous MAS peak positions, Fig. 9c, shows indications of uniaxial motional averaging, while the main amorphous peak, Fig. 9d, shows a strongly reduced anisotropy, due to near-isotropic motions in the amorphous layers.

Figure 10 displays a stacked plot of the SUPER spectrum of semicrystalline isotactic poly(1-butene), iPB, with the structure also shown in the figure. The crystallites in this sample were in the stable modification, form I. Due to mobility in the amorphous regions, the observed signals derive mostly from the ordered crystalline regions. In Fig. 11, the detailed SUPER-based CSA analysis for iPB is demonstrated. The MAS spectrum, Fig. 11a, shows four bands, for the four carbon sites in the repeat units, with 0.7 ppm splittings for each of the two types of $CH_2$ groups (*35, 36*). In spite of the relatively small number of sites, the deconvolution of the static powder spectrum in Fig. 11b had proved difficult before (*36*). The SUPER cross sections in Figs. 11c and 11d indicate why: The powder patterns of all four sites are of similar width and heavily overlapped. Our analysis shows, for instance, that the $CH_2$(b) pattern ends near 24 ppm, where the $CH_3$ pattern begins (see Figs. 11d and 11e); as a result, the

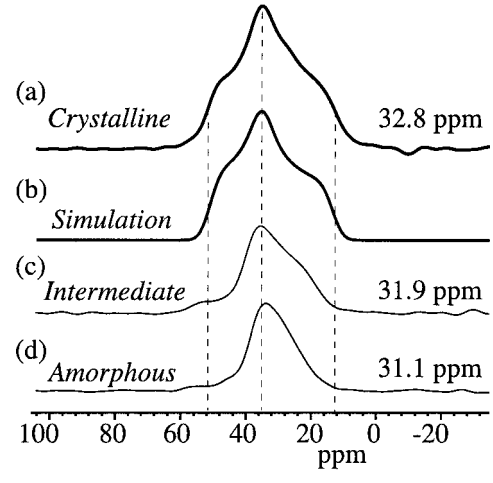


**FIG. 9.** Cross sections from a 2D SUPER spectrum of polyethylene, taken at $\omega_r/2\pi = 2.5$ kHz. (a) Powder spectrum of the *all-trans* (crystallite) peak at 32.8 ppm. (b) Corresponding simulation. (c) Cross section at 31.9 ppm, with indications of uniaxial motional averaging. (d) Cross section in the amorphous band, showing extensive motional narrowing of the CSA lineshape.

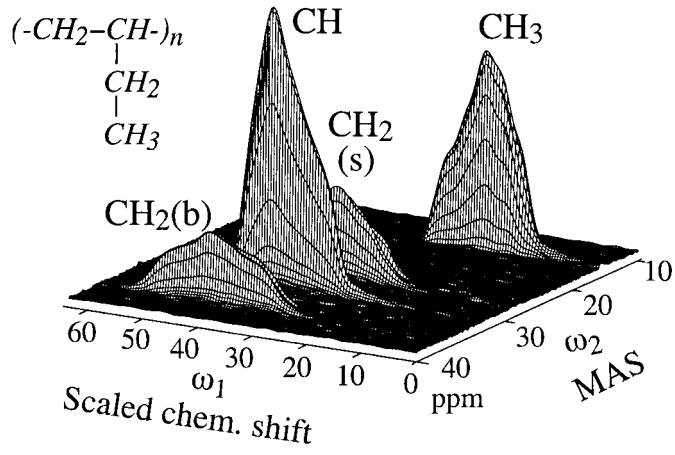


**FIG. 10.** Stacked plot of a 2D SUPER spectrum of iPB (crystal form I), taken at $\omega_r/2\pi = 2.5$ kHz. The spectrum was partially sheared by $\xi' - \chi'$, which will provide a quasi-static projection onto the $\omega_1$ axis (see Fig. 11 below). The four main bands are labeled; $CH_2$(b) and $CH_2$(s) refer to backbone and sidegroup methylenes, respectively.

corresponding steps at the ends of the powder patterns do not show up in the sum pattern, and the corresponding principal values remain impossible to determine from the static pattern alone.

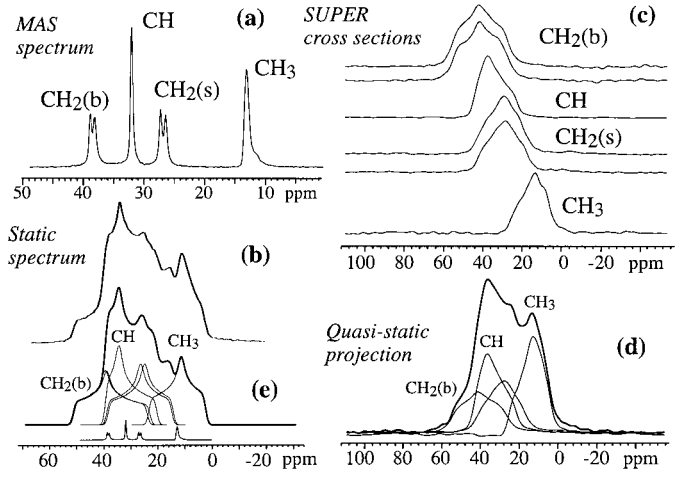


**FIG. 11.** $^{13}C$ spectra of iPB (crystal form I). (a) MAS spectrum obtained as the projection of the 2D SUPER spectrum, shown in Fig. 10, onto the $\omega_2$ axis. The splittings of the $CH_2$ resonances have been attributed to packing effects (*35*). (b) Static powder pattern. (c) SUPER cross sections at the six peak maxima of the MAS spectrum in (a). (d) Projection of the quasi-static sheared SUPER spectrum (with residual isotropic scaling factor equal to the anisotropic scaling factor). Partial projections, for each of the four bands in the spectrum in (a), are also shown. (e) Simulation of the static powder pattern shown in (b), based on the experimental deconvolution in (d). The underlying six powder patterns are also shown; the $CH_2$ patterns were scaled up by a factor of 2 for clarity. The interleaving of the powder patterns in (d) and (e) matches well. The patterns in (e) were obtained by reproducing the experimental powder patterns from (c) and (b) with less line broadening, and with variation of the CSA principal values by ±1 ppm to optimize the match with the static powder pattern in (b).

**TABLE 3**

**Chemical-Shift Principal Values and Isotropic Chemical Shifts, in ppm from Tetramethyl Silane, of the Aliphatic Carbons of Polyethylene (PE) and Isotactic Poly(1-butene) (iPB), Form I, Obtained from the Spectra Shown in Figs. 9 and 11**

| Compound name/site | $\sigma_{11}$ (ppm) | $\sigma_{22}$ (ppm) | $\sigma_{33}$ (ppm) | $\sigma_{iso}$ (ppm) |
|---|---|---|---|---|
| PE | 51 | 35 | 13 | 32.8 |
| **PE literature** | **50** | **36.5** | **12.5** | **32.8** |
| iPB: $CH_2$(backbone)-site 1 | 52 | 40 | 24.5 | 38.9 |
| iPB: $CH_2$(backbone)-site 2 | 51.5 | 39.5 | 23.5 | 38.1 |
| iPB: CH | 40 | 34.5 | 21.5 | 32.0 |
| iPB: $CH_2$(sidegroup)-site 1 | 39.5 | 27 | 15.5 | 27.3 |
| iPB: $CH_2$(sidegroup)-site 2 | 39 | 25.5 | 15 | 26.4 |
| iPB: $CH_3$ | 24 | 12 | 3 | 13.0 |

*Note.* Error margins are ±1 ppm for the values directly from the SUPER patterns, and ±0.5 ppm for values fine-tuned to match the static CSA spectrum.

In spite of the significant line broadening in the SUPER compared to the static spectrum, the SUPER data as shown in Fig. 11d make it easy to assign the various features in the static pattern of Fig. 11b. The fit and underlying six powder patterns are shown in Fig. 11e, to be compared with the experimental pattern in Fig. 11b. Some of the deviations between the overall patterns in Figs. 11b, 11d, and 11e are due to background from the amorphous regions. While the amorphous-component signal is decreased by intermediate-rate mobility for the $CH_2$ and CH groups, the $CH_3$ groups are moving fast enough to make a significant signal contribution that pushes up the peak of the methyl resonance in the experimental spectra.

*Comparison of CSA principal values.* Tables 2 and 3 summarize the chemical-shift principal values of $sp^2$- and $sp^3$-hybridized carbons, respectively, obtained by determining the inflection points ($\sigma_{11}$ and $\sigma_{33}$) as well as the maximum position ($\sigma_{22}$) of the SUPER spectra. The theoretical scaling factor was calculated to be 0.155, which includes a 3% correction arising from the $\Delta\chi'/\chi'$ contribution to the average Hamiltonian, as plotted in Fig. 4a. The agreement with available literature values is good. The COO/CON $sp^2$-carbon principal values deviate by $\leq\pm3$ ppm from the literature values, while the accuracy for the aromatic-carbon principal values is estimated to be ±5 ppm, and that of the aliphatic carbons is ±1 ppm. For many applications, e.g., the identification of chemical groups demonstrated above, this accuracy is fully sufficient.

*Conditions for $sp^2$- vs $sp^3$-hybridized carbons.* In order to obtain undistorted powder patterns, it is advisable to record 2D SUPER spectra separately for $sp^2$- and $sp^3$-hybridized carbons. The $sp^3$-carbons need good $^1H$ decoupling, due to their strong C–H couplings and small CSAs. This is achieved at a smaller MAS frequency $\omega_r$, reduced $\gamma_C B_{1,C}$, and increased relative proton decoupling field strength $\gamma_H B_{1,H}/\gamma_C B_{1,C}$. The small CSAs of $sp^3$-hybridized carbons are fully compatible with the reduced spectral width of $\sim$2.5 kHz/0.155 = 16 kHz. On the other hand, due to their large CSAs, $sp^2$-carbons require a

sufficiently large effective spectral width $\omega_r/\chi'$. In this work, we used 5 kHz/0.155 = 32 kHz or 4 kHz/0.155 = 26 kHz. Protonated aromatics are most challenging, since they require sufficiently strong $^{13}C$ $B_1$ fields to dominate the large chemical-shift anisotropy, as well as good proton decoupling. In a 2.5-mm coil, at $\omega_r/2\pi = 6$ kHz and $k = 2$ decoupling, good SUPER patterns of protonated aromatic carbons have been obtained (*37*).

Off-resonance effects represent another important reason for measuring spectra separately for $sp^2$- and $sp^3$-hybridized carbons. In a single spectrum encompassing both regions, some peaks would be nearly 100 ppm off-resonance. In our spectrometer, an off-resonance frequency of 100 ppm corresponds to 10 kHz, which leads to an $\sim 10^\circ$ tilt of the effective field and to corresponding error terms in the pulse sequence and resulting spectrum.

*Robustness and sensitivity.* The SUPER technique is very insensitive to pulse-length errors. Good carboxyl-group powder patterns were obtained on full rotors, with the sample extending to the ends of the coil, i.e., into regions where a nominal 180° pulse in the center of the coil is an $\sim 90^\circ$ pulse. The spinning speeds of 2–10 kHz at which the method is quite easily applicable due to the intrinsic accommodation of finite pulse lengths provide good flexibility. This permits the use of sample rotors of relatively large volumes at speeds that compress the signal intensities of $sp^2$-carbon sites mostly into the centerband. The combination with TOSS provides for simple MAS spectra under all conditions.

The sensitivity of the SUPER technique is high; the only reduction is from "$t_1$ noise" and similar signal-proportional artifacts. For cases where sensitivity is relevant, i.e., for samples with low intrinsic sensitivity, these artifacts are unimportant. Compared to PHORMAT (*21*), measuring times can be kept much shorter, because in the SUPER technique, the isotropic-shift dimension, which needs many time points to define sharp peaks that are spread over a wide range, is directly detected. With 32 $t_1$ points being sufficient to define a powder pattern, the minimum total number of scans in the SUPER experiment is only 1024.

The SUPER experiment is not suitable for highly $^{13}C$-labeled compounds, since the 360° pulses recouple the $^{13}C$ homonuclear dipolar interaction. As in all CSA measurements, heteronuclear couplings, for instance, to $^{15}N$ or $^{14}N$, will modify the powder pattern observed. They can be removed by an inversion pulse on the heteronucleus in the middle of the $t_1$ evolution time (which reduces the spectral width in $\omega_1$ to $\omega_r/2$).

*Comparison with other CSA separation techniques.* The (nameless) CSA recoupling technique of Bax *et al.* (*16*) (which we will refer to as the "Bax experiment" in the following), from which the 360° pulse aspect of the SUPER method has been derived, has produced respectable powder patterns (*16*). However, for scaling factors $\chi'' > 0.1$, distortions of the powder lineshapes occur in the Bax experiment, which require significant corrections to the principal values determined from the spectra. The ratio of ($^{13}C$ pulse duration)/$(\chi'' * t_r) = 1$ is more favorable in the Bax technique than in the SUPER experiment. On the other hand, the requirement of squeezing two 360° pulses into the short period $\chi'' * t_r$ of the Bax technique becomes hard to meet at the high MAS frequencies and small $t_r$ required in modern high fields. For instance, with a scaling factor of $\chi'' = 0.1$ and a spinning frequency of 3.5 kHz, the $^{13}C$ radiofrequency field strength must be $2/0.1 * 3.5$ kHz = 70 kHz, and the $^1H$ field strength ideally >140 kHz. Larger scaling factors, which would alleviate this conflict, should not be used because of the lineshape distortions and due to prohibitive broadening of the scaled aromatic powder patterns beyond the available spectral range. At 5 kHz and $\chi'' = 0.1$, the $^{13}C$ radiofrequency field would need to be as high as 100 kHz.

The resolution in the SUPER aromatic-carbon powder patterns is not as high as in PHORMAT spectra (*5*). However, it is sufficient to identify the aromatic carbons as such and distinguish them from olefinic carbons; see Figs. 7 and 8. It will also be useful to separate aromatics from the $sp^3$-hybridized O–C(RR′)–O carbons, which overlap with aromatics in the range 95–112 ppm, but have much smaller CSAs. The aromatic-carbon principal values can still be identified with better than 5% accuracy from the SUPER spectra. Better resolution should be achievable by using higher decoupling power and spinning speeds than we applied here.

The most precise determination of chemical-shift principal values can be achieved by the specialized, slow-spinning PHORMAT technique (*21*) derived from magic-angle hopping and simpler magic-angle turning experiments (*20, 38*), where the chemical shift is observed under essentially static conditions, without any scaling. However, the low sensitivity and extremely low (~25 Hz) spinning frequencies have so far restricted those techniques to very few laboratories that are dedicated to CSA measurements. In addition, obtaining high enough isotropic chemical-shift resolution to resolve, for instance, the splitting of the $CH_2$ signals in iPB, see Fig. 11, is time-consuming with the PHORMAT technique (*21*). For routine applications, the convenience of the SUPER technique is expected to represent a crucial advantage.

*Assessment and outlook.* The considerable number of experimental powder patterns shown in this paper testifies to the convenience and sensitivity of the SUPER method. It can be set up in 15 min, and a 9-h overnight run is fully sufficient to produce good sensitivity even for amorphous polymers with broad MAS lines. The data analysis consists fundamentally in reading off the $\sigma_{22}$ peak position and the $\sigma_{11}$ and $\sigma_{33}$ inflection points in a standard powder pattern. The accuracy found by comparison with the literature is good. The SUPER method thus represents a practical NMR tool for identifying chemical groups and detecting fast dynamics as part of standard MAS investigations. Lineshape analysis for site-resolved orientation measurements in oriented samples such as polymer fibers and films will also be feasible with this technique. For characterizing

molecular conformation, it can be used in conjunction with ab initio chemical-shift calculations.

The robust CSA separation technique shown here also promises to make existing "static" $^{13}$C NMR techniques, such as 2D exchange NMR or DECODER (*1*), applicable to complex organic materials, with a third, isotropic-chemical-shift dimension for site resolution. Due to the compression of the signals into sharp MAS lines and the applicability to relatively large-volume (~7-mm-outer-diameter) rotors at their highest spinning speeds, the sensitivity loss from the extra dimension in the experiments will be limited.

## CONCLUSIONS

We have introduced separation of undistorted powder patterns by effortless recoupling (SUPER), a robust NMR technique for obtaining quasi-static chemical-shift anisotropy powder patterns under MAS. With almost full rotors, standard spinning speeds, and moderate decoupling power levels, useful CSA powder patterns of CO, aromatic, olefinic, and aliphatic sites have been obtained, including the strongly dipolar coupled methylene groups of polyethylene and isotactic poly(1-butene). The only nonstandard aspect of the SUPER method, shearing of the data to avoid aliasing in the $\omega_1$ dimension, is not essential since sites of interest can be measured near resonance, or cross sections can be extended periodically. Separate measurement of the groups at >90 ppm, with higher spinning speed, and of alkyl groups at <110 ppm, with lower MAS frequency, is recommended. In sites without motion, no simulations are necessary, since the principal values of the chemical-shift tensor can be read off the measured powder patterns directly with a ruler or cursor. We have demonstrated that the CSA measured in SUPER NMR spectra can be directly useful for distinguishing COOC esters from other COO or from CON groups, or olefinic sites from aromatic C=C residues. The examples shown for glassy polymers indicate the effects of dynamics that are to be expected and can be taken into account in spectral simulations. The SUPER experiment will make CSA measurements under standard MAS conditions routine, and promises to provide many opportunities for improved structural identification and measurements of segmental orientation, conformation, and dynamics in solids.

## EXPERIMENTAL

*NMR parameters.* Experiments were performed in a Bruker DSX400 spectrometer at 100 MHz for $^{13}$C, using a 7-mm magic-angle-spinning probehead at standard spinning speeds of 2.5 kHz for $sp^3$-hybridized carbons, 4 kHz for aromatic and olefinic carbons, and 5 kHz for COO/CON carbons. For the $\chi' = 0.155$ scaling factor used throughout this work, the $^{13}$C field strength of the 360° pulses is $\gamma_C B_{1,C} = 12.12\omega_r$. The $^1$H decoupling power was increased up to $\gamma B_{1,H}/2\pi = 75$ kHz during the $^{13}$C pulses, except in experiments specifically aimed at the COO/CON sites, where a 30-kHz decoupling field was sufficient. The quality of the $^1$H decoupling during the SUPER evolution can be checked efficiently in a one-dimensional test: A 180° pulse applied at the center of the evolution time refocuses the $^{13}$C chemical-shift evolution, and the height of the resulting Hahn echo reflects the dipolar dephasing due to the residual $^1$H–$^{13}$C couplings. During detection, TPPM decoupling was applied. No tune-up of the spectrometer, other than determination of the 90° pulse lengths, was performed for the experiments. The spectral patterns are found to be quite insensitive to the exact radiofrequency strength of the $^{13}$C pulses (within at least ±15%) during the CSA recoupling. The MAS frequency was controlled by a commercial feed-back controller; rotation synchronization was achieved simply by careful pulse timing, not by triggering.

The number of $t_1$ increments was between 24 and 64 (typically 32) for $sp^2$-carbons, and 80 for $sp^3$-sites, with 32–128 scans averaged per $t_1$ increment, or a total number of scans per 2D experiment of about 4096. No TPPM decoupling was applied during the $t_1$ evolution time. Since the signal dephasing is dominated by the effects of the C–H dipolar couplings during the $^{13}$C pulses, TPPM decoupling during the windows between the $^{13}$C pulses does not result in significantly improved resolution. During simultaneous irradiation on $^{13}$C and $^1$H, 360° $^1$H pulses are expected to produce better decoupling than the 180° pulses of TPPM.

In all experiments, four-pulse total suppression of sidebands (TOSS) (*10*) was applied before detection. It was combined with an incrementation of the preceding $z$ period in four steps of $t_r/4$, which provides the "$\gamma$ integral" that suppresses sidebands up to fourth order (*39*). For $\omega_r < |\sigma_{11} - \sigma_{33}|/2$, the CSA lineshapes observed will not be perfect powder patterns, since some differential suppression of signals from different segmental orientations occurs. However, as long as the centerband is larger than the sidebands, this will lead only to an overall modulation of the CSA powder lineshape, not to a change in the positions of the steps and the maximum on the spectrum, from which the chemical-shift principal values are determined.

*Samples.* All samples extended over the full 1-cm length of the radiofrequency (rf) coil. While a few filled the whole rotor, in most cases a simple spacer made of compacted Teflon tape was placed at the bottom of the rotor to prevent parts of the sample from being placed outside the rf coil.

Fumaric acid monomethyl ester and sodium acetate were purchased from Aldrich. As a nontoxic low-molar-mass crystalline compound with an aromatic ring and a methyl group for faster relaxation, *m*-anisamide (3-methoxy benzamide) was chosen and purchased from Fluka. $^{13}$COO-labeled glycine and alanine were obtained from Cambridge Isotopes and measured simultaneously as a powder mixture for convenience; their COO peaks in the MAS spectrum are nearly baseline-resolved. The syntheses of partially $^{13}$COO-labeled PET and PEMA have been described elsewhere (*27, 28, 40*). Glassy bisphenol-A polycarbonate (PC), glassy polystyrene (PS), semicrystalline

isotactic poly(1-butene) (iPB), and semicrystalline high-density polyethylene (PE) were obtained as commercial plastics and formed into 5.5-mm cylinders by processing from the melt. The PE material was crystallized in a controlled fashion, isothermally at 130°C for several hours. The crystallites in the iPB sample had converted completely to the stable form I during months of storage at ambient temperature.

## ACKNOWLEDGMENTS

This work was partially supported by the Director for Energy Research, Office of Basic Energy Science, in the Materials Chemistry Program of Ames Laboratory, which is operated for the U.S. Department of Energy by Iowa State University under Contract W-7405-Eng-82. We thank H. W. Spiess for making the $^{13}$C-labeled PEMA sample available, and E. R. deAzevedo and T. J. Bonagamba for providing the static spectrum of iPB.

## REFERENCES

1. K. Schmidt-Rohr and H. W. Spiess, "Multidimensional Solid-State NMR and Polymers," 1st ed., Academic Press, London (1994).
2. A. C. deDios and E. Oldfield, Ab initio study of the effects of torsion angles on carbon-13 NMR chemical shielding in *N*-formyl-L-alanine amide, *N*-formyl-L-valine amide, and some simple model compounds: Applications to protein NMR spectroscopy, *J. Am. Chem. Phys.* **116,** 5307–5314 (1994).
3. J. Heller, D. D. Laws, M. Tomaselli, D. S. King, D. E. Wemmer, A. Pines, R. H. Havelin, and E. Oldfield, Determination of dihedral angles in peptides through experimental and theoretical studies of $\alpha$-carbon chemical shielding tensors, *J. Am. Chem. Soc.* **119,** 7827–7831 (1997).
4. M. Hong, Solid-state NMR determination of $^{13}$C$\alpha$ chemical shift anisotropy for the identification of protein secondary structure, submitted for publication.
5. J. Z. Hu, M. S. Solum, C. M. V. Taylor, R. J. Pugmire, and D. M. Grant, Structural determination in carbonaceous solids using advanced solid state NMR techniques, *Energy Fuels* **15,** 14–22 (2001).
6. C. J. Hartzell, M. Whitfeld, T. G. Oas, and G. P. Drobny, Determination of the $^{15}$N and $^{13}$C chemical shift tensors of L-[$^{13}$C]alanyl-L-[$^{15}$N]alanine from the dipole-coupled powder patterns, *J. Am. Chem. Soc.* **109,** 5966–5969 (1987).
7. R. H. Havlin, H. Le, D. D. Laws, A. C. deDios, and E. Oldfield, An ab initio quantum chemical investigation of carbon-13 NMR shielding tensors in glycine, alanine, valine, isoleucine, serine, and threonine: Comparisons between helical and sheet tensors, and the effects of $\chi_1$ on shielding, *J. Am. Chem. Soc.* **119,** 11951–11958 (1997).
8. T. M. Duncan, "A Compilation of Chemical Shift Anisotropies," Farragut, Chicago (1990).
9. J. Herzfeld and A. E. Berger, Sideband intensities in NMR spectra of samples spinning at the magic angle, *J. Chem. Phys.* **73,** 6021–6030 (1980).
10. W. T. Dixon, NMR spectra in spinning samples (TOSS), *J. Chem. Phys.* **77,** 1800 (1982).
11. O. N. Antzutkin, S. C. Shekar, and M. H. Levitt, 2D sideband separation in MAS NMR, *J. Magn. Reson. A* **115,** 7–19 (1995).
12. D. W. Alderman, G. McGeorge, J. Z. Hu, R. J. Pugmire, and D. M. Grant, A sensitive, high resolution magic angle turning experiment for measuring chemical shift tensor principal values, *Mol. Phys.* **95,** 1113–1126 (1998).
13. H. Geen and G. Bodenhausen, Pure absorption-mode chemical exchange NMR spectroscopy with suppression of spinning sidebands in a slowly rotating solid, *J. Chem. Phys.* **97,** 2928–2937 (1992).
14. J. Titman, S. Féaux de la Croix, and H. W. Spiess, Structure and order in solids by 3D MAS NMR, *J. Chem. Phys.* **98,** 3816 (1993).
15. A. Bax, N. M. Szeverenyi, and G. E. Maciel, Chemical shift anisotropy in powdered solids studied by 2D Fourier transform NMR with flipping of the spinning axis, *J. Magn. Reson.* **55,** 494–497 (1983).
16. A. Bax, N. M. Szeverenyi, and G. E. Maciel, Chemical shift anisotropy in powdered solids studied by 2D FT CP/MAS NMR, *J. Magn. Reson.* **51,** 400–408 (1983).
17. T. Terao, T. Fujii, T. Onodera, and A. Saika, Switching-angle sample-spinning NMR spectroscopy for powder-pattern-resolved 2D spectra: Measurement of $^{13}$C chemical-shift anisotropies in powdered 3,4-dimethoxybenzaldehyde, *Chem. Phys. Lett.* **107,** 145–148 (1984).
18. R. Tycko, G. Dabbagh, and P. Mirau, Determination of chemical-shift-anisotropy lineshapes in a two-dimensional magic-angle-spinning NMR experiment, *J. Magn. Reson.* **85,** 265–274 (1989).
19. Y. Ishii and T. Terao, Manipulation of nuclear spin Hamiltonians by rf-field modulations and its applications to observation of powder patterns under magic-angle spinning, *J. Chem. Phys.* **109,** 1366–1374 (1998).
20. Z. H. Gan, Isotropic–anisotropic correlation in rotating solids, *J. Am. Chem. Soc.* **114,** 8307 (1992).
21. J. Z. Hu, W. Wang, F. Liu, M. S. Solum, D. W. Alderman, R. J. Pugmire, and D. M. Grant, CSA separation by the PHORMAT experiment, *J. Magn. Reson. A* **133,** 210 (1995).
22. Z. H. Gan, D. M. Grant, and R. R. Ernst, NMR chemical shift anisotropy measurements by RF driven rotary resonance, *Chem. Phys. Lett.* **254,** 349–357 (1996).
23. J. D. Gross, P. R. Gross, and R. G. Griffin, Tilted *n*-fold symmetric radiofrequency pulse sequences: Applications to CSA and heteronuclear dipolar recoupling in homonuclear dipolar coupled spin networks, *J. Chem. Phys.* **108,** 7286–7293 (1998).
24. T. M. de Swiet, M. Tomaselli, and A. Pines, NMR spectra with peaks at the principal values of the chemial shielding tensor, *Chem. Phys. Lett.* **285,** 59–63 (1998).
25. L. Frydman, G. C. Chingas, Y. K. Lee, P. J. Grandinetti, M. A. Eastman, G. A. Barrall, and A. Pines, Variable-angle correlation spectroscopy in solid-state nuclear magnetic resonance, *J. Chem. Phys.* **97,** 4800 (1992).
26. Y. Ishii, J. Ashida, and T. Terao, $^{13}$C–$^{1}$H dipolar recoupling in $^{13}$C multiple-pulse solid-state NMR, *Chem. Phys. Lett.* **246,** 439–445 (1995).
27. H. Kaji and F. Horii, Analyses of local order in PET in the glassy state by 2D solid-state $^{13}$C spin diffusion NMR spectroscopy, *J. Chem. Phys.* **109,** 4651–4658 (1998).
28. A. S. Kulik, H. W. Beckham, K. Schmidt-Rohr, D. Radloff, U. Pawelzik, C. Boeffel, and H. W. Spiess, Coupling of the alpha and beta processes in poly(ethyl methacrylate) invesitgated by multidimensional NMR, *Macromolecules* **27,** 4746–4754 (1994).
29. A. Pines, M. G. Gibby, and J. S. Waugh, Proton-enhanced NMR of dilute spins in solids, *J. Chem. Phys.* **59,** 569–590 (1973).
30. J. Schaefer, M. D. Sefcik, E. O. Stejskal, R. A. McKay, W. T. Dixon, and R. E. Cais, Molecular motion in glassy polystyrenes, *Macromolecules* **17,** 1107–1117 (1984).
31. H. W. Spiess, *in* "Advances in Polymer Science" (H. H. Kausch and H. G. Zachmann, Eds.), Vol. 66, pp. 24–57, Springer-Verlag, Berlin (1985).
32. J. Schaefer, E. O. Stejskal, D. Perchak, J. Skolnick, and R. Yaris, Molecular mechanisms of the ring-flip processes in polycarbonate, *Macromolecules* **18,** 368–373 (1985).
33. D. L. VanderHart, Influence of molecular packing on solid-state $^{13}$C chemical shifts: The *n*-alkanes, *J. Magn. Reson.* **44,** 117–125 (1981).
34. K. Schmidt-Rohr, M. Wilhelm, A. Johansson, and H. W. Spiess, Determination of chemical-shift tensor in methylene groups by separated-local-field NMR, *Magn. Reson. Chem.* **31,** 352–356 (1993).

*35*. L. A. Belfiore, F. C. Schilling, A. E. Tonelli, A. J. Lovinger, and F. A. Bovey, Magic angle spinning carbon-13 NMR spectroscopy of three crystalline forms of isotactic poly(1-butene), *Macromolecules* **17** (1984).

*36*. H. W. Beckham, K. Schmidt-Rohr, and H. W. Spiess, *in* "Multidimensional Spectroscopy of Polymers" (M. W. Urban and T. Provder, Eds.), Vol. 598, pp. 243–253, Am. Chem. Soc., Washington, DC (1995).

*37*. K. Saalwächter, private communication.

*38*. A. Bax, N. M. Szeverenyi, and G. E. Maciel, Isotropic shifts and CSAs: 2D magic angle hopping NMR, *J. Magn. Reson.* **52,** 147 (1983).

*39*. E. R. deAzevedo, W.-G. Hu, T. J. Bonagamba, and K. Schmidt-Rohr, Principles of centerband-only detection of exchange in solid state NMR, and extentions to four-time CODEX, *J. Chem. Phys.* **112,** 8988–9001 (2000).

*40*. M. Dunbar, H. Kaji, E. R. deAzevedo, T. J. Bonagamba, and K. Schmidt-Rohr, unpublished.